Journal of Intelligent & Robotic Systems manuscript No.
(will be inserted by the editor)

Output Feedback Image-based Visual Servoing of Rotorcrafts

Jianan Li · Hui Xie · Rui Ma · K. H. Low

Received: date / Accepted: date

Abstract This paper presents an improved output feedback based image-based visual servoing (IBVS) law for rotorcraft unmanned aerial vehicles (RUAVs). The control law enables a RUAV with a minimal set of sensors, i.e., an inertial measurement unit (IMU) and a single downward facing camera, to regulate its position and heading relative to a planar visual target consisting of multiple points. As compared to our previous work, twofold improvement is made. First, the desired value of the image feature of controlling the vertical motion of the RUAV is a function of other image features instead of a constant. This modification helps to keep the visual target stay in the camera's field of view by indirectly adjusting the height of the vehicle. Second, the proposed approach simplifies our previous output feedback law by reducing the dimension of the observer filter state space while the same asymptotic stability result is kept. Both simulation and experimental results are presented to demonstrate the performance of the proposed controller.

Keywords Rotorcraft UAV · Image-based Visual Servoing · Virtual Camera · Nonlinear Backstepping Control

Jianan Li · K. H. Low
School of Mechanical and Aerospace Engineering, Nanyang Technological University, Singapore
E-mail: JIANAN001@e.ntu.edu.sg, MKHLOW@ntu.edu.sg

Hui Xie
School of Data and Electrical Engineering, University of Technology Sydney, Level 8, Building 11, Ultimo, NSW 2007, Australia
E-mail: Hui.Xie@uts.edu.au

Rui Ma
College of Mechanical and Electrical Engineering, Nanjing University of Aeronautics and Astronautics, China E-mail: marui@nuaa.edu.cn

1 Introduction

To regulate the relative position and heading of a rotorcraft unmanned aerial vehicle (RUAV) to a target of interest, the pose measurement from a global positioning system (GPS) aided inertial navigation system (INS) is often used. However, in some situations, GPS signals are not available, e.g., indoor condition and signal interference. Visual servoing [1] provides a potential alternative that controls the motion of a vehicle with the visual information of the target from an onboard camera. Visual servoing of UAVs is usually categorized into position-based visual servoing (PBVS) [2–9] and image-based visual servoing (IBVS) [10–16]. IBVS is usually considered easier to implement since it avoids the need for prior 3-D modelling of the target and pose reconstruction which requires more precise camera calibration [17]. Considering the benefits of IBVS mentioned in [1, 16], this paper selects the IBVS approach.

The first motivation of this paper is to improve the existing IBVS approaches by removing the velocity information requirement. Existing IBVS approaches usually require the measurement of linear velocity of the UAV, which is mostly obtained from the GPS or a motion capture system. To avoid the use of such external measuring units, some IBVS methods obtain velocity information from the optical flow measurement. For example, the works in [18, 19] apply optical flow to estimate a scaled linear velocity with the same spherical image moment features proposed in [10]. The work in [20] combines attitude measurement obtained from an inertial measurement unit and spherical optical flow to estimate the scaled translational velocity of the UAV in inertial frame. A nonlinear adaptive trajectory tracking controller is then designed to enable the UAV to land on a ship deck, which ensures the global asymp-

totic stability of the system. Besides using extra optical flow sensors, output feedback method is also adopted. In [21, 22], the authors use spherical moment features and an observer to calculate the translational velocity of the UAV. The desired value of depth is used as a nominal value for actual depth appearing in the observer. Both simulation and experimental results show the robustness of the observer to the unknown depth value. This work requires desired depth information as shown above but does not give a rigorous robustness analysis for choosing the desired depth value. In [23] the spherical image moment features and output feedback method are used for the design of IBVS control laws. Similar work is shown in [24] where an output feedback controller is proposed based on a set of first order image moment features of points in a virtual camera. It is further extended that the UAV is able to track a moving target in [25,26] using a virtual camera and an adaptive output feedback controller. Works in [23–26] prove global asymptotic stability of the system theoretically but are not experimentally validated, which is probably because of the resulting complicated controller structure.

Another issue is that as pointed out in [16], the thrust coefficient, which is an aerodynamic constant, is reduced as the battery voltage drops, and the resulting decrease in thrust has a noticeable effect on the vertical motion of the UAV. Moreover, the image feature errors tend to converge to nonzero steady state errors if there exists attitude measurement bias, which has been experimentally shown in [16]. Recently in [27, 28], an output feedback image-based visual servoing law for UAVs is proposed to adapt various system uncertainties mentioned above including reduction in thrust and attitude bias.

As in [24–28], this paper selects the virtual camera based IBVS method due to its simple and decoupled structure while similar performance can be achieved with other non-virtual camera-based approaches [29]. The chosen virtual camera has the same position and heading as the real camera but zero roll and pitch angles, and the resulting image kinematics only depends on the translational velocity and yaw rate, which recovers the passivity property of UAV dynamics [16]. This paper further extends the work in [27, 28] by removing an observer filter which is used to estimate the effect of constant disturbances while the proposed controller is still robust to disturbances, which originate from system uncertainties. The preliminary results are presented in [30]. Another contribution of this paper is that a state dependent desired feature for the vertical motion is proposed. This desired image moment feature value indirectly enables the vehicle to raise its height when the visual target is getting closer to the margin of camera's field of view (FoV). The increase of vehicle's height lets the image of visual target move towards the center of image sensor and therefore helps to keep the visual target staying in the camera's FoV. The third contribution is that experimental results are provided to show the improved performance of the proposed visual servoing law, which should be compared to many other works where only simulation results are given.

This paper is structured as follows. Section 2 describes reference coordinate frames, dynamics of the quadrotor and a vector of image moment features with its kinematics. Section 3 presents the details of the adaptive output feedback IBVS controller. The stability proof is presented in details. Simulation and experimental results are given in Section 4 and Section 5, respectively. Finally, Section 6 concludes the paper.

2 Dynamic IBVS Modeling

As shown in Fig. 1, the dynamic IBVS modeling includes a quadrotor equipped with a downward looking camera and a visual target consisting of a set of coplanar points on the ground. To describe the dynamics of the model, three reference coordinate systems are defined. A navigational frame $\mathcal{N}$ is fixed at the target's

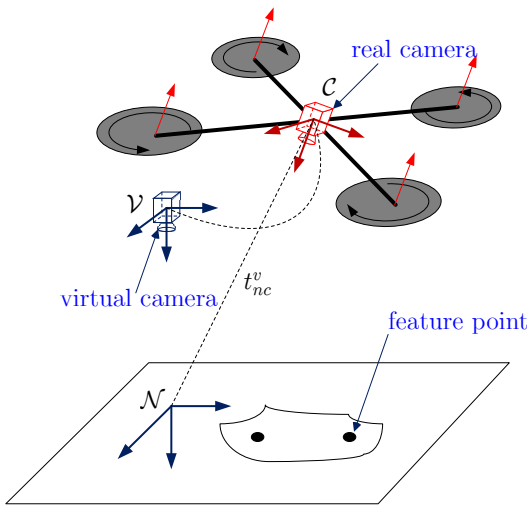

Fig. 1 Frame definition. Although the frame $\mathcal{V}$ and $\mathcal{N}$ share the same origin, to clearly show the idea of virtual camera the two frames are plotted with an offset.

plane and assumed to be inertial. A real camera frame $\mathcal{C}$ with its origin at the optical center is fixed on the quadrotor. A virtual camera frame $\mathcal{V}$ has its origin at the optical center of the camera but with zero roll and

pitch angles, which means the virtual image plane is always parallel to the target plane. The purpose of introducing the virtual camera frame is to define a set of image features in this virtual camera. The image feature kinematics of the defined features does not depend on the roll and pitch motion of the vehicle, which recovers the passivity property of UAV dynamics and simplifies the controller design due to the resulting decoupled structure [16].

The image moment feature vector $s = [s_l^T, s_h, s_\phi]^T$ of the target is defined as the same as in [27]. To illustrate the whole IBVS dynamic model, the kinematics of the image moment feature s and the quadrotor's dynamics are combined as the following:

$$\dot{s}_l = -\frac{\lambda v_l}{Z^{v*}} - D s_l \dot{\psi} \tag{1a}$$

$$\dot{s}_3 = -\frac{v_3^v}{Z^{v*}} \tag{1b}$$

$$\dot{s}_4 = -\dot{\psi} \tag{1c}$$

$$\dot{v}^v = -S(\dot{\psi}E_3)v^v + gE_3 + \frac{F^v}{m} \tag{1d}$$

$$\dot{R} = RS(\omega^c) \tag{1e}$$

$$\dot{\omega}^c = -J^{-1}S(\omega^c)J\omega^c + J^{-1}\tau^c \tag{1f}$$

where the first three equations represent the image moment features' kinematics and the latter three describe the quadrotor's dynamics; $v^v = [v_l^T, v_3^v]^T = [v_1^v, v_2^v, v_3^v]^T$ is the linear velocity expressed in $\mathcal{V}$; ω^c is the angular velocity of the camera in $\mathcal{C}$; λ is the focal length of the camera; Z^{v*} is the desired depth value of the target plane in $\mathcal{V}$; g is the gravity constant; m is the mass of the vehicle; J is the inertia of the vehicle; $E_3 = [0, 0, 1]^T$ and $D = \begin{bmatrix} 0 & -1 \\ 1 & 0 \end{bmatrix}$ are two constant matrices; R is the transformation matrix between $\mathcal{N}$ and $\mathcal{V}$ and parameterized by Euler angles $\eta = [\phi, \theta, \psi]$; the map $S(\cdot) : \mathbb{R}^3 \mapsto \mathbb{R}^{3\times 3}$ yields a skew symmetric matrix that verifies $S(x)y = x \times y$, for x and $y \in \mathbb{R}^3$; the force in frame $\mathcal{V}$ is $F^v = -R_{\theta\phi}E_3T_M$, T_M is the sum of four propellers' thrust and approximated as $T_M = K_T u_h = K_T \sum_{i=1}^4 \tilde{W}_i^2$, $\tilde{W}_i^2 = W_i - W_{min}$, W_i is the PWM signal fed into the ESC driving ith propeller, W_{min} is the minimum pulse width to start the propeller and K_T is the thrust constant, τ^c is the moment generated by propellers.

As the same as in [16, 27], a cascade control structure is adopted for visual servoing control. In this structure, the outer IBVS loop receives the image moment features of the target as the input and outputs the attitude and thrust references to regulate the image moment feature errors. The inner loop tracks the received attitude reference. As in previous work [16, 28, 31], to simplify the controller's design, the inner loop takes a PID controller and is assumed to have large enough bandwidth to ensure the stability of the whole closed-loop system. To avoid the target leaving the camera's FoV [31], IBVS control requires that the reference roll-pitch angles are limited to a small range. Therefore, a small angle approximation can be made [16] and F^v becomes

$$F^v \approx K_T u_h \begin{bmatrix} -\theta_m + \theta_e \\ \phi_m - \phi_e \\ -1 \end{bmatrix} \tag{2}$$

where ϕ_e and θ_e denote the slowly time-varying bias errors in Euler angle estimates from an attitude and heading reference system (AHRS); ϕ_m and θ_m are measured roll and pitch angles. The bias errors ϕ_e and θ_e will be treated as additive input disturbances to the outer-loop and compensated by the method of adaptive control. The thrust constant will be treated as an unknown constant parameter since it will slowly decrease as the battery voltage drops during a flight, as shown in [16]. More details of modeling, two-loop control structure and system uncertainties can be found in [16, 27].

3 Outer-loop Dynamic IBVS Control

3.1 Lateral Subsystems

In this paper, the yaw rate is assumed to be zero. We remark that this assumption is not restrictive as the yaw rate can be easily stabilized. With the assumption above and using (1a), (1d), and (2), the lateral subsystem can be written as

$$\dot{s}_i = -\frac{\lambda v_i^v}{Z^{v*}},\ i = 1, 2 \tag{3a}$$

$$\dot{v}_1^v = \frac{K_T u_h}{m}(\theta_e - \theta_m) \tag{3b}$$

$$\dot{v}_2^v = \frac{K_T u_h}{m}(\phi_m - \phi_e) \tag{3c}$$

In pitch and roll subsystems, we use ξ_1 and η_1 to denote the image moment feature errors, respectively. The pitch subsystem is written as

$$\dot{\xi} = A_0\xi + b_p B(u_\xi - d_p) \tag{4a}$$

$$y_\xi = C\xi \tag{4b}$$

where $\xi = [\xi_1, \xi_2]^T \in \mathbb{R}^2$, ξ_1 represents s_1 in (3), ξ_2 denotes $\lambda v_1^v / Z^{v*}$ in (3), y_ξ is the output variable, b_p and d_p are unknown constants dependent on K_T, m and θ_e, u_ξ is equivalent to θ_m in (3), and

$$A_0 = \begin{bmatrix} 0 & -1 \\ 0 & 0 \end{bmatrix},\ B = \begin{bmatrix} 0 \\ 1 \end{bmatrix},\ C = [1\ 0]$$

Similarly, in roll subsystem, η_1 denotes the image moment feature error. The roll subsystem has the same expression form as the the pitch subsystem, which is

$$\dot{\eta} = A_0\eta + b_r B\left(u_\eta - d_r\right) \tag{5a}$$
$$y_\eta = C\eta \tag{5b}$$

where $\eta = [\eta_1, \eta_2]^T \in \mathbb{R}^2$, η_1 represents s_2 in (3), η_2 denotes $\lambda v_2^v / Z^{v*}$ in (3), y_η is the output variable, b_r and d_r are unknown constants dependent on K_T, m and ϕ_e, u_η is equivalent to ϕ_m in (3).

3.2 Height Subsystem

From (1b), (1d), and (2), the height subsystem can be separated out and written as

$$\dot{s}_3 = -\frac{v_3^v}{Z^{v*}} \tag{6a}$$
$$\dot{v}_3^v = \frac{K_T}{m}\left(\frac{mg}{K_T} - u_h\right) \tag{6b}$$

where u_h is the input of the subsystem in (6). The objective for the height subsystem is to regulate the image moment feature error $e_{s_3} = s_3 - s_3^*$ to be zero, where s_3^* is the desired value of s_3. The image moment feature s_3 becomes $s_3 = s_3^*$ when the RUAV hovers at the desired height. As the value of image moment feature s_3 tends to be s_3^*, another assumption could be made that $u_h = u_h^*$ because the variation of u_h is relatively small. u_h^* is the constant input enabling the quadrotor to hover at the desired height.

In work [30], the desired value of s_3^* is set to be a constant $s_3^* = 1$. However, there exists a problem that the target can possibly leave the camera's FoV when the RUAV has an instant large pitch or roll angle or has a large horizontal offset relative to the target. The proposed solution in this paper is that when the visual target approaches the margin of the FoV, the RUAV will raise its height automatically. In this way, the image of the target will move towards the central zone of FoV. The desired image moment feature of height subsystem is no more a constant. Instead, we treat it as a variable, and it is essentially a function of s_1 and s_2. To simplify successive derivation, a function $G(s_1, s_2)$ is defined. The above relation can be summarized as

$$s_3^* = s_3^*(G) = s_3^*(G(s_1, s_2)) \tag{7}$$

which means s_3^* is a function of G where G is a function of s_1 and s_2. The image moment feature error in height subsystem is denoted as ζ_1, and ζ_2 denotes v_3^v / Z^*. To remain consistent with the unified lateral subsystems, the height subsystem can be rearranged as

$$\dot{\zeta} = A_0\zeta + bB(u - d) + C^T \frac{\partial s_3^*}{\partial G}\left(\frac{\partial G}{\partial s_1}\xi_2 + \frac{\partial G}{\partial s_2}\eta_2\right) \tag{8a}$$
$$y_\zeta = C\zeta \tag{8b}$$

where $\zeta = [\zeta_1, \zeta_2]^T \in \mathbb{R}^2$, ζ_1 represents $s_3 - s_3^*$ in (6), ζ_2 denotes v_3^v / Z^{v*} in (6), y_ζ is the output variable, b and d are unknown constants dependent on K_T, m, g, and Z^{v*}, u is equivalent to u_h in (6).

3.3 Control Law for Lateral Subsystems

The adaptive output feedback dynamic IBVS control law for lateral subsystems is the same as in work [27]. For completeness, the control law for pitch subsystem is shown below again. One can refer to [27] for the details of the proof. The estimate for a quantity ξ is denoted as $\hat{\xi}$ and $\tilde{\xi} = \hat{\xi} - \xi$ is its estimation error. The estimate of ξ is designed as

$$\hat{\xi} = \hat{\xi}_y + b_p\hat{\xi}_u \tag{9}$$

where $\hat{\xi_y} = [\hat{\xi}_{y1}, \hat{\xi}_{y2}]^T$, $\hat{\xi}_u = [\hat{\xi}_{u1}, \hat{\xi}_{u2}]^T$, and is updated by

$$\dot{\hat{\xi}}_y = A_o\hat{\xi}_y - L_pC\left(\hat{\xi}_y - \xi\right) \tag{10a}$$
$$\dot{\hat{\xi}}_u = A_o\hat{\xi}_u - L_pC\hat{\xi}_u + Bu_\xi \tag{10b}$$

where $L_p = [l_{1p}, -l_{2p}]^T$, l_{ip}, $i = 1, 2$ is a positive constant. Note that the integration term in [27] which is used for countering constant disturbance is removed in this observer design. However, the controller is still proven to be able to stabilize the system. Using (4a), (9), and (10), we can easily prove $\dot{\tilde{\xi}} = A_{cl}(\tilde{\xi} - H_p)$ where $H_p = [H_{1p}, H_{2p}]^T = b_p d_p[-1/l_{1p}, l_{1p}/l_{2p}]^T$, $\tilde{\xi} = [\tilde{\xi}_1, \tilde{\xi}_2]^T$, $A_{cl} = A_o - L_pC$ and . We remark that although the estimation error signal $(\tilde{\xi} - H_p)$ exponentially converges to zero, (9) cannot be used to provide a state estimate as it depends on unknown constants b_p and d_p.

Theorem 1 *The origin of the pitch system described in* (4) *with filters in* (10)*, the following adaptive output feedback control law*

$$u_\xi = -l_{2p}\hat{\xi}_{u1} + \operatorname{sgn}(b_p)\gamma_1\delta_1 w_1^T w_1 + \hat{\vartheta}_1^T q - \left(k_2 + d_2\left(k_1 + d_1\right)^2\hat{\vartheta}_{11}^2\right)\delta_2 - \hat{\vartheta}_2^T w_2$$
$$\dot{\hat{\vartheta}}_1 = \operatorname{sgn}(b_p)\gamma_1\delta_1 w_1$$
$$\dot{\hat{\vartheta}}_2 = \gamma_2\delta_2 w_2$$

where

$$\begin{aligned}
\delta_1 &= \xi_1 \\
w_1 &= [(k_1+d_1)\delta_1 - \hat{\xi}_{y2}, l_{1p}/l_{2p}]^T \\
q &= [-(k_1+d_1)\hat{\xi}_{y2} - l_{2p}\left(\hat{\xi}_{y1}-\xi_1\right), 0]^T \\
\delta_2 &= \hat{\xi}_{u2} - \hat{\vartheta}_1^T w_1 \\
w_2 &= [\hat{\vartheta}_{11}(k_1+d_1)\hat{\xi}_{u2} - \delta_1, -\hat{\vartheta}_{11}(k_1+d_1)l_{1p}/l_{2p}]^T
\end{aligned}$$

$$\operatorname{sgn}(x) = \begin{cases} 1, & x>0 \\ -1, & x<0 \\ 0, & x=0 \end{cases}$$

k_i, d_i, γ_i, $i=1,2$ are positive control gains and variables $\hat{\vartheta}_1$, $\hat{\vartheta}_2$ are the estimates of variables $\vartheta_1 = [\frac{1}{b_p}, d_p]^T$, $\vartheta_2 = [b_p, b_p d_p]^T$, respectively, is globally asymptotically stable.

Due to the symmetry of the quadrotor, the control law for roll subsystem u_η is designed exactly the same but with different notations for L_p and H_p, i.e., in the roll subsystem, the L_p is replaced by $L_r = [l_{1r}, -l_{2r}]^T$, l_{ir}, $i=1,2$ and H_p is replaced by H_r as

$$H_r = [H_{1r}, H_{2r}]^T = b_r d_r [-1/l_{1r}, l_{1r}/l_{2r}]^T.$$

3.4 Control Law for Height Subsystems

The control law for height subsystem is designed differently because s_3^* is dependent on s_1 and s_2. The estimate of ζ is designed as

$$\hat{\zeta} = \hat{\zeta}_y + b\hat{\zeta}_u - C^T s_3^* \tag{11}$$

where $\hat{\zeta}_y = [\hat{\zeta}_{y1}, \hat{\zeta}_{y2}]^T, \hat{\zeta}_u = [\hat{\zeta}_{u1}, \hat{\zeta}_{u2}]^T$, and is updated by

$$\dot{\hat{\zeta}}_y = (A_o - LC)(\hat{\zeta}_y - C^T s_3^*) + LC\zeta \tag{12a}$$

$$\dot{\hat{\zeta}}_u = (A_o - LC)\hat{\zeta}_u + Bu \tag{12b}$$

where $L = [l_1, -l_2]^T$, l_i, $i=1,2$ is a positive constant. From (8), (11) and (12), it can be proved that $\dot{\tilde{\zeta}} = A_{cl}(\tilde{\zeta} - H)$, where $\tilde{\zeta} = [\tilde{\zeta}_1, \tilde{\zeta}_2]^T$, $A_{cl} = A_o - LC$ and $H = [H_1, H_2]^T = bd[-1/l_1, l_1/l_2]^T$. Although the estimation error signal $(\tilde{\zeta} - H)$ exponentially converges to zero, we remark that (11) cannot be used to provide a state estimate as it depends on unknown constants b and d.

Theorem 2 *The origin of the system described in* (8) *with filters in* (12)*, the adaptive output feedback control law*

$$\begin{aligned}
u =& -l_2\hat{\zeta}_{u1} - \gamma_1\delta_1(w_1^T w_1 + w_2^T w_2 + w_3^T w_3) - \hat{\theta}_1^T q \\
&+ \hat{\theta}_{21} X(l_{2p}\hat{\xi}_{u1} + u_\xi) + \hat{\theta}_{31} Y(l_{2r}\hat{\eta}_{u1} + u_\eta) \\
&- Q_1\hat{\xi}_{y2} - Q_2\hat{\eta}_{y2} - \hat{\theta}_4^T w_4 - \hat{\theta}_5^T w_5 - \hat{\theta}_6^T w_6 \\
&- \left[k_2 + d_2 Q_1^2 + d_2 Q_2^2 + d_2\hat{\theta}_{11}^2 K^2\right]\delta_2
\end{aligned} \tag{13}$$

$$\dot{\hat{\vartheta}}_1 = \gamma_1\delta_1 w_1,\ \dot{\hat{\vartheta}}_2 = \gamma_1\delta_1 w_2,\ \dot{\hat{\vartheta}}_3 = \gamma_1\delta_1 w_3 \tag{14}$$

$$\dot{\hat{\vartheta}}_4 = \gamma_2\delta_2 w_4,\ \dot{\hat{\vartheta}}_5 = \gamma_2\delta_2 w_5,\ \dot{\hat{\vartheta}}_6 = \gamma_2\delta_2 w_6 \tag{15}$$

where

$$\delta_1 = \zeta_1 \tag{16}$$

$$\begin{aligned}
w_1 =& [\hat{\zeta}_{y2} - X\hat{\zeta}_{y2} - Y\hat{\eta}_{y2} - K\delta_1, l_1/l_2]^T \\
w_2 =& [-\hat{\xi}_{u2}X, \frac{l_{1p}}{l_{2p}}X]^T,\ w_3 = [-\hat{\eta}_{u2}Y, \frac{l_{1r}}{l_{2r}}Y]^T \\
w_4 =& [\hat{\theta}_{11}K\hat{\zeta}_{u2} - \delta_1, -\hat{\theta}_{11}K\frac{l_1}{l_2}]^T \\
w_5 =& [Q_1\hat{\xi}_{u2}, -Q_1\frac{l_{1p}}{l_{2p}}]^T,\ w_6 = [Q_2\hat{\eta}_{u2}, -Q_2\frac{l_{1r}}{l_{2r}}]^T \\
q =& [l_2(\hat{\zeta}_{y1} - s_3^*) - l_2\zeta_1 - Xl_{2p}(\hat{\xi}_{y1} - \xi_1) \\
&- Yl_{2r}(\hat{\eta}_{y1} - \eta_1) + K\hat{\zeta}_{y2}, 0]^T \\
\alpha =& [-M_1\hat{\xi}_{y2} - N\hat{\eta}_{y2} - 2d_1\delta_1 XM_1 \\
&- 2d_1\delta_1 NY - KX, 0]^T \\
\beta =& [-N\hat{\xi}_{y2} - M_2\hat{\eta}_{y2} - 2d_1\delta_1 YM_2 \\
&- 2d_1\delta_1 NX - KY, 0]^T
\end{aligned}$$

$$\delta_2 = \hat{\xi}_{u2} + \hat{\vartheta}_1^T w_1 + \hat{\vartheta}_2^T w_2 + \hat{\vartheta}_3^T w_3 \tag{17}$$

$$\begin{aligned}
X =& \frac{\partial s_3^*}{\partial G}\frac{\partial G}{\partial \xi_1},\ Y = \frac{\partial s_3^*}{\partial G}\frac{\partial G}{\partial \eta_1} \\
K =& k_1 + d_1 + d_1X^2 + d_1Y^2 \\
M_1 =& -\left[\frac{\partial^2 s_3^*}{\partial G^2}\left(\frac{\partial G}{\partial \xi_1}\right)^2 + \frac{\partial s_3^*}{\partial G}\frac{\partial^2 G}{\partial \xi_1^2}\right] \\
M_2 =& -\left[\frac{\partial^2 s_3^*}{\partial G^2}\left(\frac{\partial G}{\partial \eta_1}\right)^2 + \frac{\partial s_3^*}{\partial G}\frac{\partial^2 G}{2\eta_1^2}\right] \\
N =& -\left[\frac{\partial^2 s_3^*}{\partial G^2}\frac{\partial G}{\partial \xi_1}\frac{\partial G}{\partial \eta_1} + \frac{\partial s_3^*}{\partial G}\frac{\partial^2 G}{\partial \xi_1 \partial \eta_1}\right] \\
Q_1 =& \hat{\theta}_1^T\beta - \hat{\theta}_{21}\hat{\xi}_{u2}N + \hat{\theta}_{22}\frac{l_{1p}}{l_{2p}}N \\
&- \hat{\theta}_{31}^T\hat{\eta}_{u2}M_2 + \hat{\theta}_{32}\frac{l_{1r}}{l_{2r}}M_2 \\
Q_2 =& \hat{\theta}_1^T\beta - \hat{\theta}_{21}\hat{\xi}_{u2}N + \hat{\theta}_{22}\frac{l_{1p}}{l_{2p}}N \\
&- \hat{\theta}_{31}^T\hat{\eta}_{u2}M_2 + \hat{\theta}_{32}\frac{l_{1r}}{l_{2r}}M_2
\end{aligned}$$

k_i, d_i, γ_i, $i=1,2$ are positive control gains and variables $\hat{\vartheta}_1$, $\hat{\vartheta}_2$, $\hat{\vartheta}_3$, $\hat{\vartheta}_4$, $\hat{\vartheta}_5$, $\hat{\vartheta}_6$ are the estimates of variables $\vartheta_1 = [\frac{1}{b}, d]^T$, $\vartheta_2 = [\frac{1}{b_p}, d_p]^T$, $\vartheta_3 = [\frac{1}{b_r}, d_r]^T$, $\vartheta_4 = [b, bd]^T$, $\vartheta_5 = [b_p, b_p d_p]^T$ and $\vartheta_6 = [b_r, b_r d_r]^T$, respectively, is globally asymptotically stable.

Proof. The control law is designed based on the Lyapunov theory and the backstepping technique. Set the first error as the image moment feature error δ_1 in height subsystem given in (16). Combined with (6a), (9), and (10), the derivative of the first error δ_1 becomes

$$\begin{aligned}\dot{\delta}_1 =& -\hat{\zeta}_2 + \tilde{\zeta}_2 - \dot{s}_3^* \\ =& -\hat{\zeta}_{y2} - b\hat{\zeta}_{u2} + \tilde{\zeta}_2 + \frac{\partial s_3^*}{\partial G}(\frac{\partial G}{\partial s_1}\xi_2 + \frac{\partial G}{\partial s_2}\eta_2)\end{aligned}$$

The expression of $\dot{\delta}_1$ can be also written as

$$\begin{aligned}\dot{\delta}_1 =& -K\delta_1 - b\left(\hat{\zeta}_{u2} + \theta_1^T w_1 + \theta_2^T w_2 + \theta_3^T w_3\right) \\ & - X(\tilde{\xi}_2 - H_{2p}) - Y(\tilde{\eta}_2 - H_{2r}) + (\tilde{\zeta}_2 - H_2)\end{aligned} \tag{18}$$

In the above expression of $\dot{\delta}_1$, only the time derivative of variable $\hat{\zeta}_{u2}$ contains the control input u. Thus, the variable $\hat{\zeta}_{u2}$ is selected as the virtual control input in the backstepping technique. Combined with the definition of δ_2 in (17), the expression of $\dot{\delta}_1$ can be written again as

$$\begin{aligned}\dot{\delta}_1 =& -K\delta_1 - b\left(\delta_2 - \tilde{\theta}_1^T w_1 - \tilde{\theta}_2^T w_2 - \tilde{\theta}_3^T w_3\right) \\ & - X(\tilde{\xi}_2 - H_{2p}) - Y(\tilde{\eta}_2 - H_{2r}) + (\tilde{\zeta}_2 - H_2)\end{aligned}$$

We select the first Lyapunov function as

$$\begin{aligned}V_1 =& \frac{1}{2}\delta_1^2 + \frac{|b|}{2\gamma_1}\left(\tilde{\theta}_1^T\tilde{\theta}_1 + \tilde{\theta}_2^T\tilde{\theta}_2 + \tilde{\theta}_3^T\tilde{\theta}_3\right) \\ &+ \frac{1}{d_1}\Big[(\tilde{\zeta} - H_2)^T P_{cl}(\tilde{\zeta} - H_2) + (\tilde{\xi} - H_{2p})^T P_{cl}(\tilde{\xi} - H_{2p}) \\ & + (\tilde{\eta} - H_{2r})^T P_{cl}(\tilde{\eta} - H_{2r})\Big]\end{aligned} \tag{19}$$

where P_{cl} satisfies $P_{cl}A_{cl} + A_{cl}^T P_{cl} = -I_2$, $I_2 \in \mathbb{R}^{2\times 2}$ is an identity matrix. Employing (14) and (19), the time derivative of V_1 is

$$\begin{aligned}\dot{V}_1 =& -K\delta_1^2 + b\delta_1(\tilde{\theta}_1^T w_1 + \tilde{\theta}_2^T w_2 + \tilde{\theta}_3^T w_3) \\ & - b\delta_1\delta_2 + \frac{|b|}{\gamma_1}(\tilde{\theta}_1^T\dot{\tilde{\theta}}_1 + \tilde{\theta}_2^T\dot{\tilde{\theta}}_2 + \tilde{\theta}_3^T\dot{\tilde{\theta}}_3) \\ & - \delta_1 X(\tilde{\xi}_2 - H_{2p}) - \delta_1 Y(\tilde{\eta}_2 - H_{2r}) - \delta_1(\tilde{\zeta}_2 - H_2) \\ & - \frac{1}{d_1}\Big[(\tilde{\zeta} - H_2)^T(\tilde{\zeta} - H_2) + (\tilde{\xi} - H_{2p})^T(\tilde{\xi} - H_{2p}) \\ & + (\tilde{\eta} - H_{2r})^T(\tilde{\eta} - H_{2r})\Big] \\ \leq& -k_1\delta_1^2 - b\delta_1\delta_2 + \frac{-3}{4d_1}\left[(\zeta - H)^T(\zeta - H)\right. \\ & \left. + (\xi - H_p)^T(\xi - H_p) + (\eta - H_r)^T(\eta - H_r)\right]\end{aligned} \tag{20}$$

Using the definitions of w_1 in Theorem 2 and updating laws in (12a), (12b) as well as the expression of $\dot{\delta}_1$ in (18), the time derivative of w_1 can be derived as

$$\begin{aligned}\dot{w}_1 =& q + \alpha(\hat{\xi}_2 - \tilde{\xi}_2) + \beta(\hat{\eta}_2 - \tilde{\eta}_2) + \begin{bmatrix} Kb(\hat{\zeta}_{u2} - \frac{dl_1}{l_2}) \\ 0 \end{bmatrix} \\ & + \begin{bmatrix} -K(\tilde{\zeta}_2 - \frac{bdl_1}{l_2}) \\ 0 \end{bmatrix}\end{aligned} \tag{21}$$

where q, α and β are defined in Theorem 2. The time derivative of w_2 and w_3 can be derived as

$$\dot{w}_2 = \begin{bmatrix} -X(l_{2p}\hat{\xi}_{u1} + u_\xi) - \hat{\xi}_{u2}(M_1\xi_2 + N\eta_2) \\ \frac{l_{1p}}{l_{2p}}(M_1\xi_2 + N\eta_2) \end{bmatrix} \tag{22}$$

$$\dot{w}_3 = \begin{bmatrix} -Y(l_{2r}\hat{\eta}_{u1} + u_\eta) - \hat{\eta}_{u2}(M_2\eta_2 + N\xi_2) \\ \frac{l_{1r}}{l_{2r}}(M_2\eta_2 + N\xi_2) \end{bmatrix} \tag{23}$$

where the definitions of X, Y, M_1, M_2 and N are listed in Theorem 2. The time derivative of the second error δ_2 is obtained by using (10b), (14) and (21)-(23).

$$\begin{aligned}\dot{\delta}_2 =& l_2\hat{\zeta}_{u1} + u + \gamma_1\delta_1(w_1^T w_1 + w_2^T w_2 + w_3^T w_3) + \hat{\theta}_1^T q \\ & - \hat{\theta}_{21}X(l_{2p}\hat{\xi}_{u1} + u_\xi) - \hat{\theta}_{31}Y(l_{2r}\hat{\eta}_{u1} + u_\eta) \\ & + Q_1\hat{\xi}_{y2} + Q_2\hat{\eta}_{y2} + \vartheta_4^T w_4 + \vartheta_5^T w_5 + \vartheta_6^T w_6 \\ & - Q_1(\tilde{\xi}_2 - H_{2p}) - Q_2(\tilde{\eta}_2 - H_{2r}) - \hat{\theta}_{11}K(\tilde{\zeta}_2 - H_2) \\ & + b\delta_1\end{aligned} \tag{24}$$

The second Lyapunov function is selected as

$$\begin{aligned}V_2 =& V_1 + \frac{1}{2}\delta_2^2 + \frac{1}{2\gamma_2}(\tilde{\theta}_4^T\tilde{\theta}_4 + \tilde{\theta}_5^T\tilde{\theta}_5 + \tilde{\theta}_6^T\tilde{\theta}_6) \\ & + \frac{1}{d_2}\Big[(\tilde{\zeta} - H)^T P_{cl}(\tilde{\zeta} - H) + (\tilde{\xi} - H_p)^T P_{cl}(\tilde{\xi} - H_p) \\ & + (\tilde{\eta} - H_r)^T P_{cl}(\tilde{\eta} - H_r)\Big]\end{aligned}$$

Employing (15), (20) and (24), the time derivative of V_2 can be obtained as

$$\begin{aligned}\dot{V}_2 =& -k_1\delta_1^2 - b\delta_1\delta_2 + \delta_2\Big[l_2\hat{\zeta}_{u1} + u + \hat{\theta}_1 q \\ & + \gamma_1\delta_1(w_1^T w_1 + w_2^T w_2 + w_3^T w_3) \\ & - \hat{\theta}_{21}X(l_{2p}\hat{\xi}_{u1} + u_\xi) - \hat{\theta}_{31}Y(l_{2r}\hat{\eta}_{u1} + u_\eta) \\ & + Q_1\hat{\xi}_{y2} + Q_2\hat{\eta}_{y2} - \hat{\theta}_{11}K(\tilde{\eta}_2 - H_2) + b\delta_1 \\ & + \hat{\theta}_4^T w_4 + \tilde{\theta}_4^T w_4 + \hat{\theta}_5^T w_t - \tilde{\theta}_5^T w_5 + \hat{\theta}_6^T w_6 - \tilde{\theta}_6^T w_6 \\ & - Q_1(\tilde{\xi}_2 - H_{2p}) - Q_2(\tilde{\eta}_2 - H_{2r})\Big] \\ & + \frac{1}{\gamma_2}(\tilde{\theta}_4^T\dot{\tilde{\theta}}_4 + \tilde{\theta}_5^T\dot{\tilde{\theta}}_5 + \tilde{\theta}_6^T\dot{\tilde{\theta}}_6) \\ & - \frac{3}{4d_1}\Big[(\tilde{\zeta} - H)^T(\tilde{\zeta} - H) + (\tilde{\xi} - H_p)^T(\tilde{\xi} - H_p) \\ & + (\tilde{\eta} - H_r)^T(\tilde{\eta} - H_r)\Big] \\ & - \frac{1}{d_2}\Big[(\tilde{\zeta} - H)^T(\tilde{\zeta} - H) + (\tilde{\xi} - H_p)^T(\tilde{\xi} - H_p) \\ & + (\tilde{\eta} - H_r)^T(\tilde{\eta} - H_r)\Big]\end{aligned}$$

Finally, using the inequality $2xy \leqslant x^2 + y^2$, we can show that

$$\begin{aligned}\dot{V}_2 \leq& -k_1\delta_1^2 - \frac{3}{4d_1}\Big[(\tilde{\zeta} - H)^T(\tilde{\zeta} - H)\end{aligned}$$

$$+(\tilde{\xi}-H_p)^T(\tilde{\xi}-H_p)+(\tilde{\eta}-H_r)^T(\tilde{\eta}-H_r)\Big]$$
$$-k_2\delta_2^2-\frac{3}{4d_2}\Big[(\tilde{\zeta}-H)^T(\tilde{\zeta}-H)$$
$$+(\tilde{\xi}-H_p)^T(\tilde{\xi}-H_p)+(\tilde{\eta}-H_r)^T(\tilde{\eta}-H_r)\Big]$$

Applying the LaSalle-Yoshizawa Theorem in [32], we can show the boundedness of $\tilde{\zeta}$, δ_i, $\hat{\vartheta}_i$, $i=1,2$, and the convergence of $\hat{\vartheta}_i$, δ_i, $i=1,2,...6$ to zero. With the definition of $\hat{\zeta}_y$ and the boundedness of $\tilde{\zeta}_1$, we can prove that the values of $\hat{\zeta}_y$ are bounded. Similarly, using the definition of $\hat{\zeta}_1=\hat{\zeta}_{y1}+b\hat{\zeta}_{u1}-s_3^*$, and the boundedness of $\tilde{\zeta}_1$ and δ_1, we can conclude the boundedness of $\hat{\zeta}_1$ and $\hat{\zeta}_{u1}$. Also the definition of w_1, w_2, w_3 and δ_2, and the boundedness of δ_2, $\hat{\zeta}_{y2}$, imply the variables w_1, w_2, w_3 and $\hat{\zeta}_{u2}$ are bounded. Finally, with the boundedness of variables shown above and the proposed control law in (13), we can conclude the input u for system in (8) is bounded. □

4 Simulation Results

Numerical simulation is presented in this section to evaluate the performance of the proposed controller. In the simulation, the physical constants are set as the following: the vehicle's mass $m=1.6$ kg, inertia $J=\text{diag}([0.03,0.03,0.05])$ kg·m^2 which is estimated based on classical rotating pendulum, torque constant $K_T=20$ N·ms^2, focal length $\lambda=2.8$ mm, image sensor size 3.2 mm×2.4 mm with the resolution of 320×200 pixels. The image moment feature errors are denoted as $e_s=s-s^*=[e_{s1},e_{s2},e_{s3},e_{s4}]^T$, where the desired value is $s^*=[0,0,s_3^*,0]$. In this simulation, s_3^* is selected as

$$s_3^*=\begin{cases}1, & G\le 0.01\\ (G-0.01)+1, & G>0.01\end{cases} \tag{25}$$

where $G=2(s_1^2+s_2^2)$ for simplicity. We remark that the construction of the s_3^* function is based on the camera's performance, target's size, the sensitivity of height adjustment and other requirements. Complicated functions will increase the complexity of the control law. The desired translational displacement of the vehicle is set as $t_{nc}^{n*}=[0,0,-1.5]^T$ m. The vehicle is initially set to be hovering at $t_{nc}^n(0)=[0.2,-0.2,-1.0]^T$ m in navigational frame. Its initial attitude is set to be $[0°,0°,30°]^T$ in roll, pitch and yaw angles. The initial velocities are assumed as $v^v(0)=0$ m/s and $\omega^c(0)=0$ rad/s. The attitude bias error is $\eta_{e1}=[-1°,1.5°,0°]^T$. The visual target consists of two co-planar points on the ground located at coordinates $[-0.18,0,0]^T$ m and $[0.18,0,0]^T$ m in the navigational frame.

The outer loop control parameters for lateral subsystem are shown in Table 1. Due to the symmetry of quadrotor, the parameters for pitch and roll subsystems are the same. The control parameters for height subsystem are given in Table 2. A proportional controller for regulating the image moment feature s_4 to zero is used which is the same as in [16]. A PID controller is used for the inner attitude loop to remain consistency with the method in PX4 firmware.

Table 1 Gains for lateral subsystem in simulation

Parameter	k_1	d_1	k_2	d_2	γ_1	γ_2	l_1	l_2
Value	2.0	0.01	10	0.1	0.1	0.1	10	25

Table 2 Gains for height subsystem in simulation

Parameter	k_1	d_1	k_2	d_2	γ_1	γ_2	l_1	l_2
Value	1.2	0.01	6	0.01	0.1	0.1	7.2	9

Fig. 2 shows the time evolution of image moment feature errors $e_s=[e_{s1},e_{s2},e_{s3},e_{s4}]^T$, position errors $e_t=[e_{t_1},e_{t_2},e_{t_3}]^T$, and heading error $e_\psi=\psi-\psi^*$. We

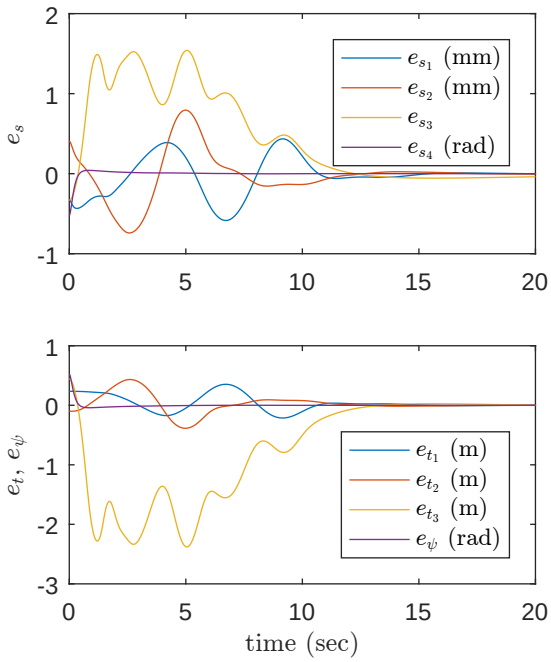

Fig. 2 Time evolution of image moment feature errors e_s and e_t

can observe that after around 10 seconds, all the errors converge to zero. This result proves the capability of the proposed controller to eliminate the steady state error

resulting from attitude bias, which is not considered in existing output feedback based IBVS laws [23, 24, 26]. It can also be observed that in the first 10 seconds, e_{s3} and e_{t3} have quite different behaviors compared to those of other two image feature errors of s_1 and s_2. This is expected and reasonable because a large lateral displacement error occurs in the first 10 seconds, which results that Theorem 2 sets the desired image moment feature s_3^* larger than 1.

The time evolutions of s_3^* and s_3 are illustrated in Fig. 3. It can be observed that the resulting s_3 is trying to follow s_3^*. As a result, the vehicle stays higher than the desired height in order to obtain a better view of the target. After the lateral displacement error becomes smaller as defined in (25), s_3^* returns to be 1, and the vehicle starts to descend from about 3.5 m to the desired height which is set as 1.5 m.

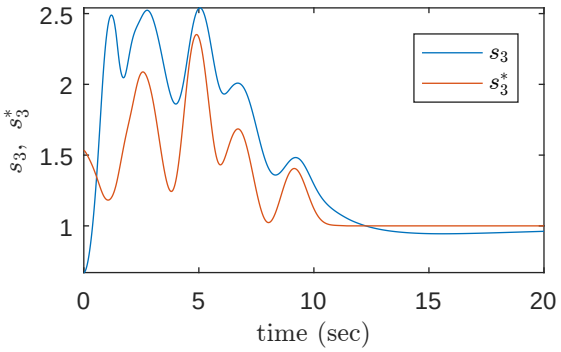

Fig. 3 Time evolution of desired image moment feature s_3^* and s_3

Fig. 4 illustrates the time evolution of reference roll and pitch signals of the vehicle given to the inner attitude loop. As expected, the reference signals are bounded. Fig. 5 depicts the trajectories of the two target's image points. It can be seen that the visual target stays in the camera's FoV. If only the controller in Theorem 1 acts on the whole system, we remark that although it guarantees the stability of the closed-loop system for any positive control gains, to practically implement the proposed control laws requires tuning control gains appropriately in order to obtain satisfactorily transient trajectories. Otherwise, the visual targets will potentially leave the camera's FoV during the transient period. However, apart from the IBVS law in Theorem 1 controlling the lateral subsystems, the IBVS law in Theorem 2 controls the height subsystem which helps to keep the target to stay in the camera's FoV.

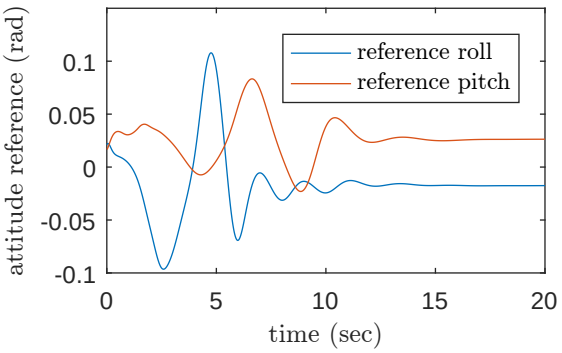

Fig. 4 Time evolution of roll and pitch reference.

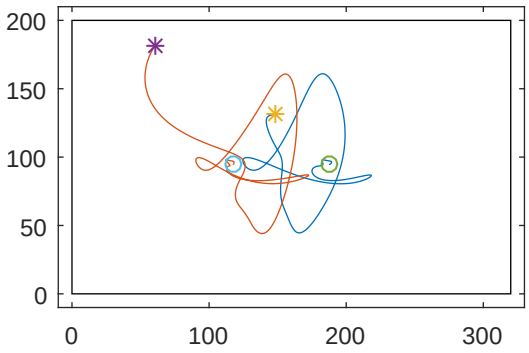

Fig. 5 Image trajectories of two target points. The symbols $*$ and $\circ$ represent the starting and end points, respectively. The rectangle shows the boundary of the image sensor.

5 Experimental Evaluation

5.1 Experimental Platform

Fig. 6 shows the configuration of the aerial vehicle used in the experiment, which is a quadrotor equipped with an open-source Pixhawk autopilot [33] and a CMUcam5 Pixy on-board computer vision system [34]. The vehicle is powered by two 11.1V 2200 mAh LiPo rechargeable batteries. The total weight of the aerial vehicle including two batteries is around 1.6 kg. The arm length of the quadrotor is 0.2 m. The commercial Pixhawk autopilot has a group of 3D accelerometers, gyroscopes

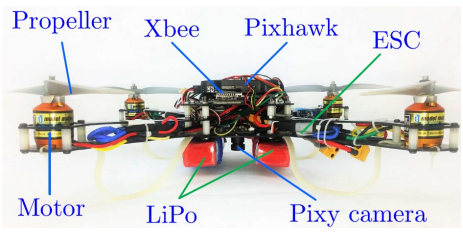

Fig. 6 The built quadrotor UAV.

and magnetometers. To estimate the attitude and angular velocity of the quadrotor, an AHRS based on extended Kalman filter is adopted for fusing IMU and magnetometer sensor data. The autopilot outputs the reference PWM signals to four ESCs, which then drive the four 840 RPM/V brushless motors mounted with $10 \times 3.8''$ multi-rotor propellers. The Pixy camera is installed at the bottom of the quadrotor for a better view of the targets. The camera's focal length is $\lambda = 2.8$ mm and image sensor size is $1/4''$. The lens of the camera has a field of view of 75° horizontally and 47° vertically. The camera module transmits image point coordinates at a rate of 25 Hz with a resolution of 320×200 pixels. More details of the implementation can be found in [16].

5.2 Experimental Results

In this experiment, the desired image moment feature in height subsystem s_3^* is set as the same as (25) in simulation. The two co-planar targets on the ground are separated by 0.45 m.

The control gains of the outer-loop in lateral and height subsystems are listed in Table 3 and Table 4, respectively. Due to the symmetry of the quadrotor, the gains are tuned the same for both pitch and roll subsystems.

Table 3 Gains for lateral subsystem in experiment

Parameter	k_1	d_1	k_2	d_2	γ_1	γ_2	l_1	l_2
Value	0.5	0.01	5	0.01	0.05	0.1	4	4

Table 4 Gains for height subsystem in experiment

Parameter	k_1	d_1	k_2	d_2	γ_1	γ_2	l_1	l_2
Value	1.2	0.01	6	0.01	0.1	0.1	7.2	9

Fig. 7 depicts the time evolution of image moment feature error which is $e_s = [e_{s1}, e_{s2}, e_{s3}, e_{s4}]^T$, and Fig. 8 shows the pose errors $e_s = [e_{t1}, e_{t2}, e_{t3}, e_\psi]^T$. Both figures suggest that the errors reach the steady state after around 20 seconds. In steady state, the errors only oscillate within a very small range where for image moment feature errors, the oscillation magnitudes are within 0.1 mm for e_{s1}, e_{s2} and e_{s4}, and 0.1 for e_{s3}; for position and heading errors, the oscillation magnitudes are less than 0.1 m and 0.1 rad, respectively. For the first 10 seconds in transition period, the errors e_{s3} and e_{t3} seem not to

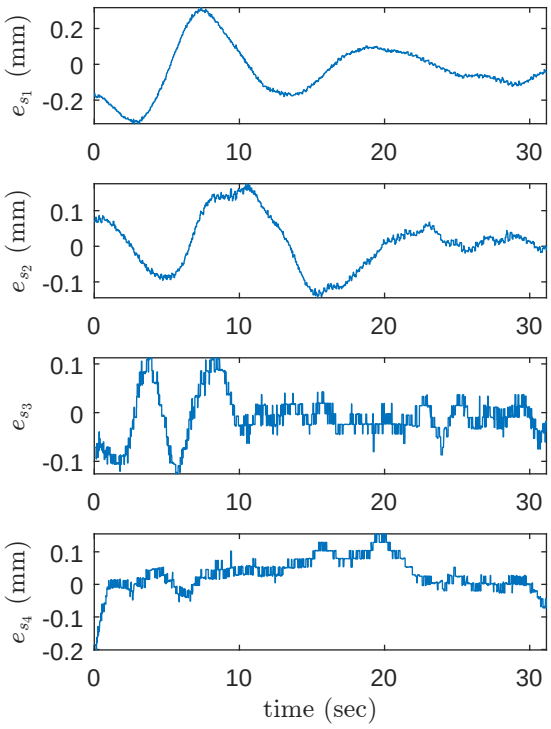

Fig. 7 Time evolution of image moment feature errors e_s

tend to converge to the steady state. This is because the position error in lateral direction is still large enough that the control law in Theorem 2 forces the vehicle to raise its height in order to track the targets in a better view. This behavior is illustrated more clearly in Fig. 9. The desired image moment feature s_3^* is computed using (25). From Fig. 9, we can find that the real time s_3 is trying to follow the desired one s_3^*. Although there exists time lag which is about 1 s, the camera keeps the target image in a certain scope to reduce the probability of losing the target image.

The time evolution of outer-loop inputs ϕ_m, θ_m and u_h are illustrated in Fig. 10. The control inputs are all bounded as expected. After around 20 seconds when the vehicle reaches its steady state, the control inputs are not zero, which proves that the proposed controller is able to eliminate the attitude bias errors. Fig. 11 shows the real time trajectory of the quadrotor in 3D view and three views. Symbol "$*$" means the starting point and "$\triangle$" stands for the ending point of the quadrotor in this experiment. Two small circles "$\circ$" denote the two co-planar target points on the ground. From the front view and side view, one can see that whenever the quadrotor flies away from the target horizontally, it will raise its height by itself. Thus, both front and side view have a rough shape like a bowl. In other words, the trajectory

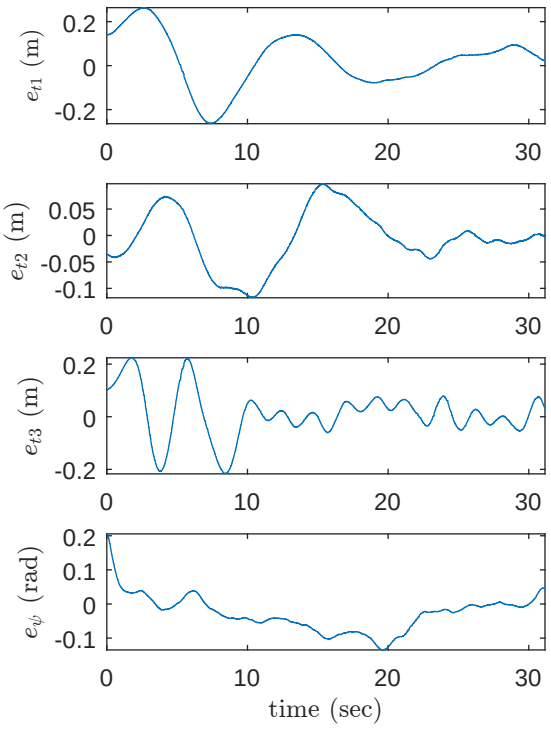

Fig. 8 Time evolution of position e_t and yaw errors e_ψ

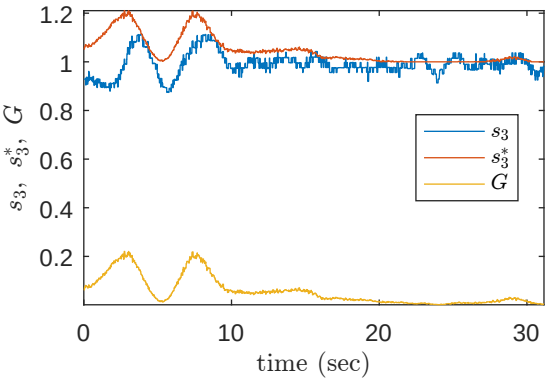

Fig. 9 Time evolution of s_3^*, s_3 and G

presents a tendency to be concave. From the top view, it can be observed that the quadrotor is away from the targets at the beginning and finally hovers above the center of the two target points within a range less than 10 cm.

6 Conclusion

An adaptive output feedback dynamic IBVS control law is proposed in this paper. The objective of the controller is to control the relative position and heading

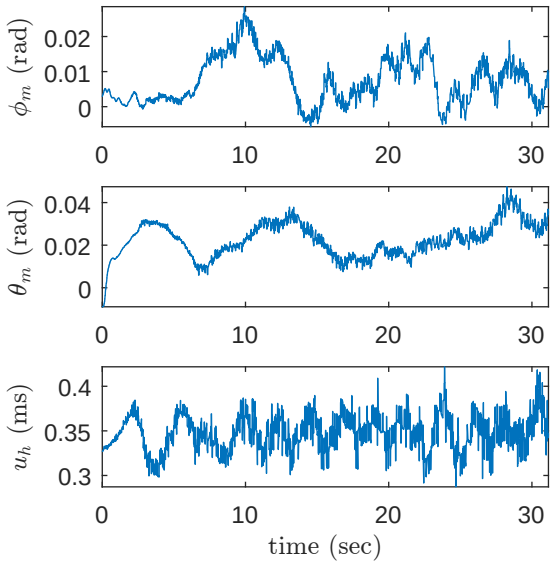

Fig. 10 Time evolution of outer-loop inputs ϕ_m, θ_m, u_h

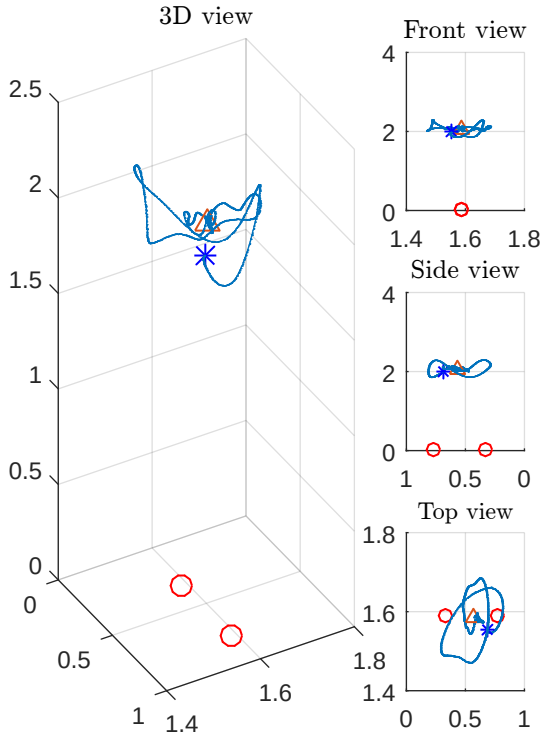

Fig. 11 Trajectory of the aerial vehicle in 3-D

between the quadrotor and a co-planar horizontal target with the help of a minimum sensor set combining an inertial measurement unit and a vision sensor. The origins of the closed-loop systems, namely the lateral and height subsystems, are proven to be asymptotically stable. Compared to our previous work, the proposed

control law is further simplified in lateral subsystem by reducing the dimension of the observer filter state space while the same asymptotic stability result is kept. For height subsystem, it is designed more intelligently that it will adjust its height to get a better view of the target through processing the information in lateral direction. Compared to other visual servoing method of UAVs, the proposed control law removes the requirement of velocity information, an estimate of depth, disturbance, known mass, and thrust coefficient, and thus is robust to the slowly varying aerodynamic thrust constant. The method is also robust to measurement bias in roll and pitch angles, and therefore has the capability of eliminating nonzero steady state errors. Both simulation and experimental results are presented to demonstrate the performance of the proposed approach. Future work includes the visual servoing of a moving target with its theory proof and experiment implementation.

Acknowledgements This work is supported by Air Traffic Management Research Institute (ATMRI) in Singapore under the ASBU project (Research Grant No. NTU-ATMRI 2014-D1-LOW).

References

1. F. Chaumette and S. Hutchinson, "Visual servo control part I: Basic approaches," *IEEE Robot. Autom. Mag.*, vol. 13, no. 4, pp. 82–90, 2006.
2. O. Shakernia, Y. Ma, T. J. Koo, and S. Sastry, "Landing an unmanned air vehicle: Vision based motion estimation and nonlinear control," *Asian J. Control*, vol. 1, no. 3, pp. 128–145, 1999.
3. E. Altug, J. Ostrowski, and C. Taylor, "Quadrotor control using dual camera visual feedback," in *Proc. 2003 IEEE Int. Conf. Robot. Autom*, vol. 3, Taipei, Taiwan, Sep. 2003, pp. 4294–4299.
4. A. D. Wu, E. N. Johnson, and A. A. Proctor, "Vision-aided inertial navigation for flight control," *J. Aerosp. Comput. Inf. Comm.*, vol. 2, no. 9, pp. 348–360, 2005.
5. L. Mejias, S. Saripalli, P. Campoy, and G. S. Sukhatme, "Visual servoing of an autonomous helicopter in urban areas using feature tracking," *J. Field Robotics*, vol. 23, no. 3-4, pp. 185–199, 2006.
6. S. Azrad, F. Kendoul, and K. Nonami, "Visual servoing of quadrotor micro-air vehicle using color-based tracking algorithm," *J. System Design and Dynamics*, vol. 4, no. 2, pp. 255–268, 2010.
7. L. García Carrillo, E. Rondon, A. Sanchez, A. Dzul, and R. Lozano, "Stabilization and trajectory tracking of a quad-rotor using vision," *J. Intell. Robot. Syst.*, vol. 61, no. 1-4, pp. 103–118, 2011.
8. E. Rondon, L.-R. Garcia-Carrillo, and I. Fantoni, "Vision-based altitude, position and speed regulation of a quadrotor rotorcraft," in *Proc. 2010 IEEE/RSJ Int. Conf. Intelligent Robots and Systems*, Taipei, Taiwan, Oct. 2010, pp. 628–633.
9. L. Carrillo, G. Flores Colunga, G. Sanahuja, and R. Lozano, "Quad rotorcraft switching control: An application for the task of path following," *IEEE Trans. Control Syst. Technol.*, vol. 22, no. 4, pp. 1255–1267, 2014.
10. T. Hamel and R. Mahony, "Visual servoing of an under-actuated dynamic rigid-body system: an image-based approach," *IEEE Trans. Robot. Autom.*, vol. 18, no. 2, pp. 187–198, 2002.
11. O. Bourquardez, R. Mahony, N. Guenard, F. Chaumette, T. Hamel, and L. Eck, "Image-based visual servo control of the translation kinematics of a quadrotor aerial vehicle," *IEEE Trans. Robot.*, vol. 25, no. 3, pp. 743–749, 2009.
12. N. Metni, T. Hamel, and F. Derkx, "Visual tracking control of aerial robotic systems with adaptive depth estimation," in *Proc. 44th IEEE Conf. Decision and Control, and the European Control Conf.*, Seville, Spain, Dec. 2005, pp. 6078–6084.
13. H. de Plinval, P. Morin, P. Mouyon, and T. Hamel, "Visual servoing for underactuated VTOL UAVs: A linear, homography-based framework," *Int. J. Robust. Nonlin.*, vol. 24, no. 16, pp. 2285–2308, 2013.
14. R. Ozawa and F. Chaumette, "Dynamic visual servoing with image moments for a quadrotor using a virtual spring approach," in *Proc. 2011 IEEE Int. Conf. Robot. Autom*, Shanghai, China, May 2011, pp. 5670–5676.
15. ——, "Dynamic visual servoing with image moments for an unmanned aerial vehicle using a virtual spring approach," *Adv. Robotics*, vol. 27, no. 9, pp. 683–696, 2013.
16. H. Xie, "Dynamic visual servoing of rotary wing unmanned aerial vehicles," Ph.D. dissertation, Dept. Electrical and Computer Engineering, University of Alberta, Edmonton, AB, 2016.
17. B. Espiau, "Effect of camera calibration errors on visual servoing in robotics," in *Experimental Robotics III*, ser. Lecture Notes in Control and Information Sciences, T. Yoshikawa and F. Miyazaki, Eds. Berlin: Springer, 1994, vol. 200, pp. 182–192.
18. R. Mahony, P. Corke, and T. Hamel, "Dynamic image-based visual servo control using centroid and optic flow features," *J. Dyn. Syst-T. ASME*, vol. 130, pp. 011 005–01–011 005–12, 2007.
19. F. L. Bras, R. Mahony, T. Hamel, and P. Binetti, "Dynamic image-based visual servo control for an aerial robot: Theory and experiments," *Int. J. Optomechatronics*, vol. 2, no. 3, pp. 296–325, 2008.
20. B. Herissé, T. Hamel, R. Mahony, and F.-X. Russotto, "Landing a VTOL unmanned aerial vehicle on a moving platform using optical flow," *IEEE Trans. Robot.*, vol. 28, no. 1, pp. 77–89, 2012.
21. R. Mebarki and B. Siciliano, "Velocity-free image-based control of unmanned aerial vehicles," in *Proc. 2013 IEEE/ASME Int. Conf. Advanced Intelligent Mechatronics*, July 2013, pp. 1522–1527.
22. R. Mebarki, V. Lippiello, and B. Siciliano, "Nonlinear visual control of unmanned aerial vehicles in GPS-denied environments," *IEEE Trans. Robot.*, vol. 31, no. 4, pp. 1004–1017, 2015.
23. F. Le Bras, T. Hamel, R. Mahony, and A. Treil, "Output feedback observation and control for visual servoing of VTOL UAVs," *Int. J. Robust. Nonlin.*, vol. 21, no. 9, pp. 1008–1030, 2011.
24. H. Jabbari Asl, G. Oriolo, and H. Bolandi, "Output feedback image-based visual servoing control of an underactuated unmanned aerial vehicle," *P. I. Mech. Eng. I.-J. Sys.*, vol. 228, no. 7, pp. 435–448, 2014.
25. H. J. Asl and J. Yoon, "Robust image-based control of the quadrotor unmanned aerial vehicle," *Nonlinear Dynam.*, vol. 85, no. 3, pp. 2035–2048, 2016.
26. A. Abdessameud and F. Janabi-Sharifi, "Image-based tracking control of VTOL unmanned aerial vehicles," *Automatica*, vol. 53, pp. 111–119, 2015.

27. H. Xie and K. H. Low, "Dynamic visual servoing of a rotary-wing unmanned aerial vehicle without velocity measurement," in *Proc. AIAA Guidance, Navigation, and Control Conf.*, Grapevine, Texas, Jan. 2017, Art. no. AIAA 2017-1745.
28. H. Xie, K. H. Low, and Z. He, "Adaptive visual servoing of unmanned aerial vehicles in GPS-denied environments," *IEEE-ASME T. Mech.*, vol. 22, no. 6, pp. 2554–2563, 2017.
29. G. Fink, H. Xie, A. F. Lynch, and M. Jagersand, "Nonlinear dynamic image-based visual servoing of a quadrotor," *J. Unmanned Veh. Syst.*, vol. 3, no. 1, pp. 1–21, 2015.
30. H. Xie, J. Li, and K.-H. Low, "Dynamic output feedback image-based visual servoing of rotorcraft UAVs," in *Proc. 2017 Int. Conf. Unmanned Aircraft Systems*, Miami, FL, June 2017, pp. 1361–1367.
31. H. Xie and A. F. Lynch, "Input saturated visual servoing for unmanned aerial vehicles," *IEEE-ASME T. Mech.*, vol. 22, no. 2, pp. 952–960, 2017.
32. M. Krstic, P. V. Kokotovic, and I. Kanellakopoulos, *Nonlinear and Adaptive Control Design*, 1st ed. New York: John Wiley & Sons, 1995.
33. L. Meier, D. Honegger, and M. Pollefeys, "PX4: A node-based multithreaded open source robotics framework for deeply embedded platforms," in *Proc. 2015 IEEE Int. Conf. Robot. Autom*, Seattle, WA, May 2015.
34. Pixy CMUcam5. Accessed 5 June 2015. [Online]. Available: http://www.cmucam.org/projects/cmucam5/wiki

Jianan Li received his joint M.Sc. degree in aerospace engineering from Technical University of Munich, Germany and Nanyang Technological University, Singapore in 2018; the B.Sc. degree in electromechanical engineering from the University of Macau, Macao, China, in 2015. His research interests include linear and nonlinear control, vision-based control and coordinated control of multiple vehicles with application to unmanned aerial vehicles with its traffic management.

Hui Xie received his B.Sc. degree in mechanical engineering from Harbin Engineering University in 2007, the M.Sc. degree in mechatronics engineering from Harbin Institute of Technology in 2009, and Ph.D. in Electrical and Computer Engineering from the University of Alberta in 2016. Currently, he is a postdoctoral research associate in the School of Electrical and Data Engineering at University of Technology Sydney.

His research interests include nonlinear control theory, state estimation, and vision-based control with applications to unmanned aerial vehicles and mobile robots.

Rui Ma received his M.E. in Solid Mechanics from Jiangsu University, China, in 2014. He is currently a Ph.D. student in Mechanical and Electrical Engineering, Nanjing University of Aeronautics and Astronautics, China. His research areas include autonomous flight control and swarm intelligent optimization with applications to unmanned aerial vehicles.

Kin Huat Low received the B.Sc. degree from National Cheng Kung University, Tainan, Taiwan, and the M.Sc. and Ph.D. degrees in mechanical engineering from the University of Waterloo, Waterloo, ON, Canada. He is currently a Professor with the School of Mechanical and Aerospace Engineering, Nanyang Technological University, Singapore.

His teaching and research interests include robotics, unmanned aerial vehicles, air traffic management, vibrations, impacts, exoskeleton systems, mechatronics design, machines, and mechanisms.